Journal of Magnetic Resonance **147,** 36–42 (2000)
doi:10.1006/jmre.2000.2186, available online at http://www.idealibrary.com on IDEAL®

Thermally Polarized ^{1}H NMR Microimaging Studies of Liquid and Gas Flow in Monolithic Catalysts

Igor V. Koptyug,* Stephen A. Altobelli,† Eiichi Fukushima,† Anatoly V. Matveev,‡ and Renad Z. Sagdeev*

*International Tomography Center, Novosibirsk 630090, Russia; †New Mexico Resonance, Albuquerque, New Mexico 87106; and ‡Novosibirsk State University, Novosibirsk 630090, Russia

Received March 21, 2000; revised August 4, 2000

The feasibility of gas flow imaging in moderately high magnetic fields employing thermally polarized gases at atmospheric pressures is demonstrated experimentally. Two-dimensional spatial maps of flow velocity distributions for acetylene, propane, and butane flowing along the transport channels of shaped monolithic alumina catalysts were obtained at 7 T by ^{1}H NMR, with true in-plane resolution of 400 μm and reasonable detection times. The resolution is shown to be limited by the echo attenuation due to rapid molecular diffusion in the imaging gradients of magnetic field. All gas flow images exhibit flow patterns that are not fully developed, in agreement with the range of Reynolds numbers (190–570) and the length of the sample used in gas flow experiments. The flow maps reveal the highly nonuniform spatial distribution of shear rates within the monolith channels of square cross-section, the kind of information essential for evaluation and improvement of the efficiency of mass transfer in shaped catalysts. The water flow images were obtained at lower Re numbers for comparison. These images demonstrate the transformation of a transient flow pattern observed closer to the inflow edge of a monolith into a fully developed one further downstream. © 2000 Academic Press

Key Words: **NMR imaging; liquid and gas flow; monolithic catalysts.**

INTRODUCTION

Reactors with packed beds of catalysts are used in catalytic steam reforming of natural gas and other hydrocarbons, air pollution prevention by catalytic combustive purification of automobile and plant exhaust, and other important industrial applications. Heat and mass transport and exchange are key elements in such heterogeneous catalytic processes. Therefore, the shape of the catalysts/supports constituting the catalyst bed can have a major impact on the efficiency of the process through its effect on flow and mixing through the bed. Indeed, one of the recent trends in large-scale industrial processes is to control the shape of catalyst/support pellets, such as monolithic catalysts possessing large transport channels, in order to reduce pressure drop while uniformly distributing flow across a reactor (*1, 2*). The design of the monoliths' shapes so far has been purely empirical, and significant improvements can be made to improve various aspects of their performance, if systematic measurements of flow and heat transfer within such structures could be made. Therefore, information on mass transport in liquid and gas flow in monolithic catalysts is highly desirable.

While the application of NMR imaging to study flow of various liquids in a wide variety of geometries is done routinely (*3*), the feasibility of gas flow NMR imaging has not been addressed in detail. There appears to be only one such publication (*4*) and it reports the application of dynamic NMR imaging of hyperpolarized ^{129}Xe to obtain joint spatial–velocity distribution maps for a tube with a constriction and for two types of polyurethane foams. The majority of gas imaging applications deal with the imaging of human and animal airways and lungs, utilizing either hyperpolarized noble gases (^{129}Xe, ^{3}He) (*5–11*) or thermally polarized gases (^{129}Xe, CF_4, C_2F_6, SF_6) (*12–14*), often mixed with O_2 in various proportions to produce breathable mixtures. A number of applications of gas imaging to materials science have also been reported, both with hyperpolarized (*4, 15*) and thermally polarized gases (*16–18*). Finally, hyperpolarized gas imaging has also been performed in a very weak magnetic field (*19*). The studies are often performed at elevated gas pressures in order to reduce the usually high diffusivity of gas molecules, to reduce the efficiency of spin-rotational relaxation, and to increase concentration. This work investigates the possibility of performing gas flow imaging with thermally polarized proton-containing gases at ambient pressures and carries out some preliminary studies of the flow of gases and liquids in the transport channels of shaped catalysts.

EXPERIMENTAL

Universal butane gas for lighters (Eurofill, Aerosols B.V., Holland) liquefied in 200-ml cans (116 g net weight) was purchased in a local tobacco store. Propane (liquefied in 5-liter tanks for domestic burners), acetylene (for torch welders), and hydrogen gas were purchased from commercial vendors. Unfortunately, information on the purity of gases was not available from the vendors. The NMR spectrum of propane exhibited several weaker (not more than a few percent total) lines at

1090-7807/00 $35.00

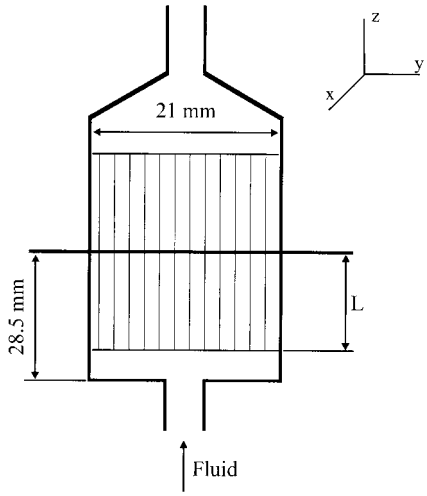

FIG. 1. The geometry of the Teflon cell containing the monoliths. *L* is the distance from the lower edge of the catalyst to the center of the imaged slice (the center of the gradient and the RF coils).

lower fields relative to the main resonances, while the other gases did not have any impurities which could be detected by proton NMR. Distilled water was used in the water flow studies. No attempt was made to reduce the relaxation time of water by doping it with paramagnetic species in order to avoid contamination of the catalysts.

The monoliths were made of γ-Al_2O_3 and had a specific surface area of 62 m^2/g and 14-nm average pore diameter as measured by the low-temperature nitrogen adsorption method. However, the permeability of the channel walls does not significantly influence the flow fields described in this study. The monoliths studied in this work had transport channels of 4 mm^2 cross-section and wall thickness of 1 mm. The roughly cylindrical pieces were cut out of bigger monoliths to fit into a 21-mm-id Teflon cell, with the orientation of the channels coinciding with the direction of the cylindrical cell axis. These monoliths were cut so that either a channel or an intersection of channel walls coincided with the center of the cylinder. It will be seen later that these two kinds of monoliths created vastly different flow patterns when the fluid inlet was a narrow jet, comparable in width to that of a channel.

The geometry of the Teflon cell and sample positioning are shown in Fig. 1. Either a single monolith, 41 mm long, or a stack of two pieces, 25 mm each, were used. In all experiments reported here, the fluids entered the cell at the bottom and exited at the top. For the gas flow experiments, a 2- to 3-m piece of 4-mm-id polyethylene tubing was attached to the cell on each end. The desired flow rate was adjusted using the valve of the float-type rotameter (preceded by the gas tank pressure regulator for H_2 and acetylene), which was calibrated for each gas with the use of a drum gas meter as well as by measuring the time necessary to displace a known volume of water from a calibrated flask. The gas expanded from the tank into the supply tubing attached to the bottom part of the cell and exited the setup through the exhaust tubing attached to the top part of the cell into the fume hood.

The cooling of the small butane gas cans upon gas expansion and the resulting gas flow rate variation in the course of the experiments was prevented by immersing the cans in a tank of water maintained at room temperature. For other gases, this was not required owing to the larger tanks. For the relaxation time measurement of gases at ca. 1 atm pressure, monoliths were removed from the Teflon cell and the flow system was flushed with the respective gas, and then the supply valve was closed, and a few seconds later the outflow tubing was closed.

For the water flow experiments, larger tubing (5.5-mm-id) was used, while the cell geometry, sample positioning, and flow direction were the same. The flow of water was created by a thermostat pump (Lauda A100) and its flow rate was measured by timed collection.

All ^{1}H NMR microimaging experiments were performed on a Bruker DRX spectrometer equipped with a vertical bore superconducting magnet at 299 MHz. A birdcage RF coil with 25-mm-id was used to accommodate the Teflon cell. The spin-echo pulse sequence with a slice-selective 90° pulse and a hard 180° pulse was employed in all experiments. Frequency and phase encoding were along the two orthogonal directions in the *x*-*y* plane perpendicular to the cell axis, and slice selection took place along the *z* axis. The slice thickness was 2 mm for water and 15 mm for gas studies. Two extra gradients were applied along the *z* axis to phase encode the flow velocity (*20*). In the gas imaging experiments, the number of scans averaged was 8 for butane, 16 for propane, and 256 for acetylene, and the original data matrix size was 64×64. For water, the number of scans was reduced to 4 and the data matrix size increased to 128×128. The field of view was 24 mm^2 in all experiments. Each 2D data set was zerofilled to 256×256 and Fourier transformed in two dimensions. For each measurement the experiment was performed twice, with and without the fluid flowing. The pixel-by-pixel phase difference was then calculated for each pair of images, and phase unwrapping was applied to those velocity maps where phase wrap occurred. Sine apodization was employed in certain cases to reduce truncation artifacts.

The magnitude of the frequency encode gradient in the gas imaging experiment was 9.3 G/cm, and the acquisition time was 690 μs. An attempt to improve spatial resolution in the gas images by doubling the gradient led to an almost complete signal loss. When imaging various gases, we kept most of the parameters of the spin-echo pulse sequence the same (including echo time, $T_E = 5.1$ ms) except for the recovery time and the number of accumulations, which were adjusted for each particular gas. In water imaging experiments the echo time was 2.7 ms. It took 20 to 40 min to acquire each 2D image.

Relaxation times of gases were measured in the Teflon cell after removing the monoliths. The T_1 times were measured by inversion-recovery, while the T_2 times were measured using the CPMG sequence. It was verified that a factor of 2 variation

in the refocusing time τ has no influence on the measured T_2 value ($\tau \ll T_2$). The measured values were reproducible to within a few percent, but the values should be considered approximate since the amount of impurities and residual air in the samples was unknown.

RESULTS

1. Liquid Flow Imaging

Figure 2 shows water flow velocity maps detected at 12.5 (Fig. 2a) and 18.5 mm (Fig. 2b) from the catalyst inflow edge. As in all other images detected, the walls and the square channels of the monoliths can be unambiguously identified. The flow enters through a small orifice on the central axis of the cylindrical sample cell. The catalyst walls cross near the axis of the cell and redirect the flow toward the sample periphery, as indicated by the flow velocity distribution in the central four channels of the sample. The flow pattern is even more complicated in the outer channels. As the positive and negative "c"-shape structures in Fig. 2a suggest, there is some kind of slow vortical motion of liquid in these channels. At the moment we are unable to say whether this is the up–down circulation or a circular flow within the image plane, and we will clarify this point in the future. However, 6 mm further downstream (Fig. 2b) the flow pattern has already developed into one which could be expected for a fully developed flow within a channel of a square cross-section, with the square flow velocity contours near the channel walls gradually transforming into the circular ones toward the channel centers. Rotating the upper block of the stack by 45° relative to the lower (imaged) one transforms the contours in at least the two channels with the highest flow velocities into arrowhead-shape structures pointing away from the center. When the flow rate is further increased, the flow direction in the outer channels is reversed, while most of the flow is still going through the central four channels (not shown).

In another series of liquid flow imaging experiments, the stack of two monoliths was supported by a third monolith having much narrower channels with cross-section of 1 mm^2. This structure could be useful for preserving the jet-type flow of liquid entering the cell. The variation of the experiment geometry and flow rate can have a strong and sometimes curious influence on the flow pattern. For example, we can change the flow rate, mutual orientation of the monoliths, and the distance, L, to reproducibly redirect most of the flow into the outer channels of the monolith. Such behavior will be studied in more detail in the future.

Figure 3 maps the flow of water through a monolith of a different geometry, with a channel in the center. In this case the main flow is observed in the central channel, while there is also measurable flow in its four nearest neighbors. A 150- to 250-μm slit in one of the walls which goes along the entire monolith is circled in the image of Fig. 3. Transverse flow-weighted images indicate that it could be inducing some flow in the plane of the image, although it does not seem to have any effect on the flow velocity distribution along the channels.

2. Gas Flow Imaging

We carried out a series of flow velocity imaging experiments with hydrogen-containing gases—molecular hydrogen (H_2), acetylene (C_2H_2), *n*-propane (C_3H_8), and *n*-butane (C_4H_{10}). The primary goal of these studies was to assess the feasibility of gas flow velocity imaging with ^1H detection of thermally polarized gases at ambient pressures and temperatures and to uncover the limitations of this approach.

Our attempts to detect images of H_2 failed, even when the echo time was reduced to 1 ms and the flow encoding gradients were eliminated. We subsequently measured the H_2 T_2 to be 0.38 ms (Table 1), too short for the signal to be detected under these experimental conditions. In addition, the large diffusivity of H_2 of 1.66 cm^2/s at 22°C and 1 atm (*21*), more than an order of magnitude larger than that of other gases used in this work, makes the signal even more elusive. Our attempt to image H_2 yielded only a weak but unmistakable image of the birdcage RF insert parts made of hydrogen-containing materials. For the three other gases, both static and flow-weighted images of reasonable quality were detected, with a true in-plane resolution of ca. 400 × 400 μm, artificially improved to 100 × 100 μm by zerofilling.

Figure 4 shows a two-dimensional axial flow velocity map of propane gas flowing through the cylindrical cell (no monoliths in the cell). It demonstrates that the geometry of our flow system is not perfectly cylindrically symmetric. In addition, the gas flows in the reverse direction at a much lower velocity outside of the jet in the center of the cell. This is shown in Fig. 5. As can be seen, the image quality is sufficiently good to warrant the application of the method to the studies of more complex flow patterns.

A flow velocity map for acetylene C_2H_2 is shown in Fig. 6 whereas Fig. 7 shows butane C_4H_{10} flowing through the same monolith. All parameters were the same in the two experiments, except for a somewhat higher flow rate for butane, and the maximum flow velocities in the images are nearly equal. Most of the flow goes through the central channels in both cases. Despite very different appearances of the flow patterns in the two images of Figs. 6 and 7 (circular vs square-shape flow velocity contours), both images indicate little interaction of the flow with the channels walls. The circular contours observed in Fig. 6 may have developed in the long gas supply tubing. The inner diameter of the latter (4 mm) is equal to the side length of the square cross-section of the channel, and the paraboloid just fits into the central channel of the monolith.

The flow in Fig. 7 has an appearance of a plug flow, with a large flow velocity gradient in the immediate vicinity of the channel walls and little variation of the rate within the rest of the channel. This type of velocity profile may be expected in

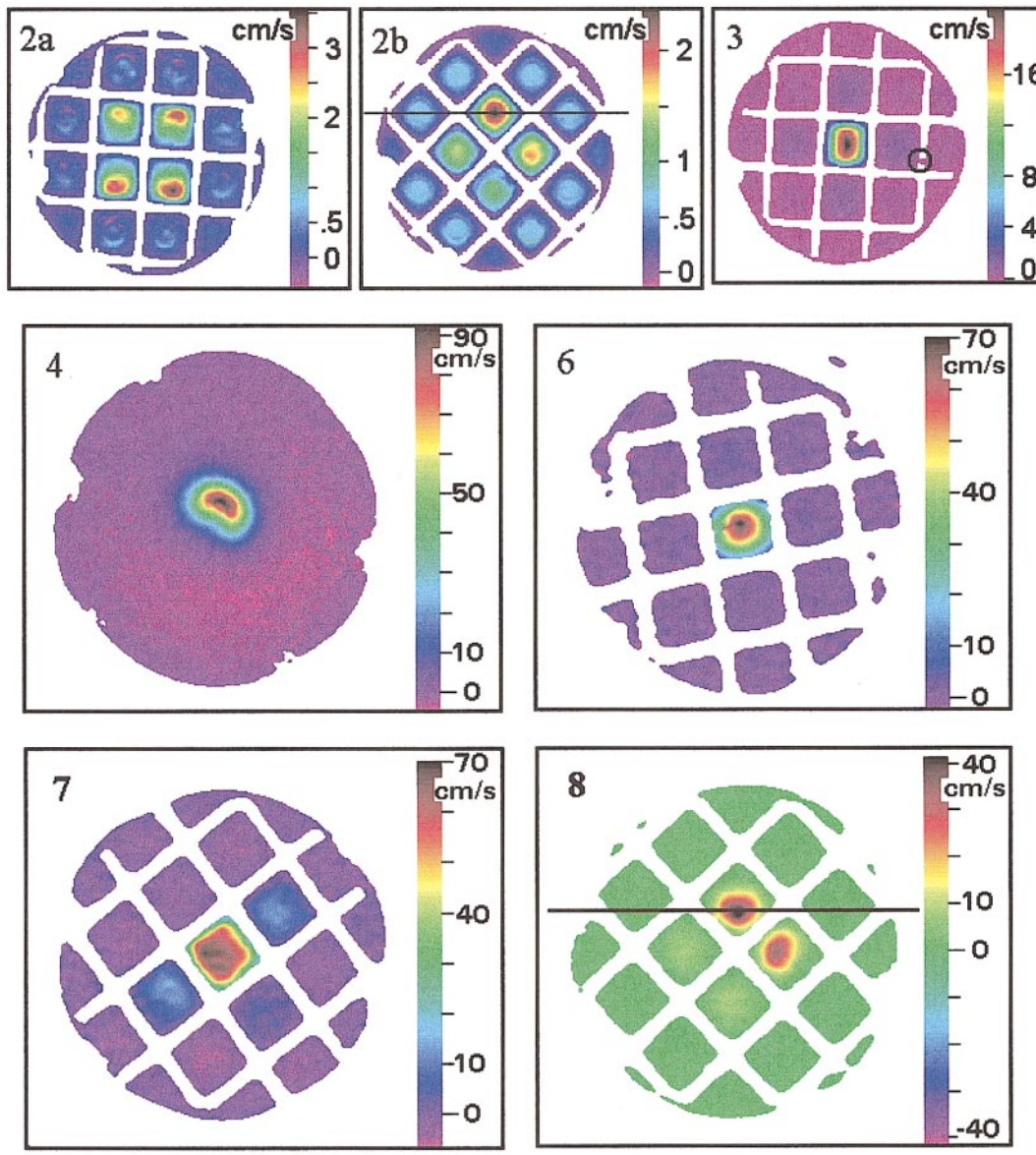

FIG. 2. Two-dimensional axial flow velocity maps of water flowing through a cylindrical cell containing a stack of two monolithic catalysts with identical orientation. (a) Distance from the monolith edge to the detected slice $L = 12.5$ mm, flow rate 69 ml/min, maximum flow velocity 3.6 cm/s; (b) $L = 18.5$ mm, flow rate 76 ml/min, maximum flow velocity 2.4 cm/s. Figure 9 shows a one-dimensional velocity profile along the dark line.

FIG. 3. Two-dimensional axial flow velocity map of water flowing through a cylindrical cell containing a monolithic catalyst with a central channel. $L = 12.5$ mm, flow rate 128 ml/min, and maximum flow velocity 21.6 cm/s. The slit in one of the monolith walls is circled.

FIG. 4. Two-dimensional axial flow velocity map of propane (C_3H_8) gas flowing through a cylindrical cell (no monoliths). Flow rate is 400 ml/min and maximum flow velocity is 93.0 cm/s.

FIG. 6. Two-dimensional axial flow velocity map of acetylene (C_2H_2), $L = 18.5$ mm, flow rate 500 ml/min, maximum flow velocity 72.0 cm/s.

FIG. 7. Two-dimensional axial flow velocity map of butane (C_4H_{10}), $L = 18.5$ mm, flow rate 375 ml/min, maximum flow velocity 70.0 cm/s.

FIG. 8. Two-dimensional axial flow velocity map of propane gas flowing through a cylindrical cell containing a stack of two monolithic catalysts with identical orientation relative to each other. $L = 18.5$ mm, flow rate 360 ml/min, maximum flow velocity 43.0 cm/s. Figure 9 shows a one-dimensional velocity profile along the dark line.

entry flow regions, where the effects of viscosity are confined to thin boundary layers adjacent to solid surfaces. The differences between Figs. 6 and 7 could be, in part, due to the factor of three difference in the kinematic viscosities of the two gases.

We thus conclude that fully developed flow within the channels is not attained in the image plane and that mapping of flow velocity distributions in longer channels is required to visualize the establishment of a fully developed flow. Although the direction of flow coincides with that of the supply tubing in the central channel and its four closest neighbors, the weak

TABLE 1
Relaxation Times of Gases Studied in This Work

Gas	T_1[a], ms	T_2[b], ms
Hydrogen (H_2)	3.1	0.38
Acetylene (H_2C_2)	205	150
Propane ($H_3C–CH_2–CH_3$)	995	586
n-Butane ($H_3C–CH_2–CH_2–CH_3$)	1270	746

[a] Inversion-recovery.
[b] CPMG.

flow in the other channels is in the opposite direction. This is in agreement with the results for the cylindrical cell with no monolith inserted (Figs. 4 and 5). We confirm also that spatial resolution in the gas images is lower than in the water images; the slit in one of the walls of the monolith circled in Fig. 3 is not resolved in the images of Figs. 6 and 7.

The perturbation of the flow is strongest when the monolith walls intersect in the center. The flow is redirected unequally into the four central channels (Fig. 8), and the spatial distribution of the flow velocity depends critically on the details of the experiment. In this particular example with propane gas, the flow velocity contours change from roughly circular to butterfly-shaped upon the increase of flow rate from 360 to 480 ml/min.

Figure 9 shows profiles of the axial component of velocity along selected lines through the color images of Figs. 2b and 8. The liquid velocity profile of Fig. 9a appears to be highly developed and shows significant flow in the outer channels. The gas velocity profile of Fig. 9b is more jet-like and shows a higher wall shear rate in the central channel and a near-zero flow in the outer channels.

DISCUSSION

Mass transfer between the monolith and the fluid flowing through its channels is expected to be most efficient in the entrance regions where flow patterns are not fully developed and the boundary layer is thin. Therefore, to assess and improve the efficiency of monolithic catalysts, a detailed knowledge of shear rates and entrance lengths in the operating model reactor is required. As the water and gas images obtained in this work demonstrate, NMR microimaging can provide such information in a nondestructive and noninvasive way. For instance, the transition from a transient flow pattern to a fully developed one is demonstrated in Fig. 2. The Reynolds numbers Re estimated from the known flow rates and assuming that water flows predominantly through the four central channels are ca. 70–80. The corresponding entrance length can be estimated as ca. 10 mm. This number is in a good agreement with the experimental observations of a transient pattern at 12.5 mm and a developed pattern at 18.5 mm. Gas flow images were detected for Re in the range 190–570 corresponding to entrance lengths of 25–70 mm. This is why the observed gas flow patterns are far from being fully developed and why significant interaction of the flowing gas with the monolith is evident only in the immediate vicinity of the channel walls.

The results reported here demonstrate the feasibility of gas flow imaging with thermally polarized hydrocarbon gases at ambient pressures, with reasonable detection times and true spatial resolution of the order of 400 μm. The diffusion-limited resolution for propane can be estimated as $(2D\tau)^{0.5}$, where $D = 0.066$ cm^2/s (*21*) is the self-diffusivity of propane at 295 K and 1 atm, and τ is the time of spatial localization of the spins in the pulse sequence employed. With $\tau = 1$ ms, the diffusion limit for the achievable spatial resolution is 115 μm. Assuming that the diffusivity of acetylene is similar to that of ethylene, the corresponding number for acetylene is 160 μm, while for butane this value should be approximately 100 μm.

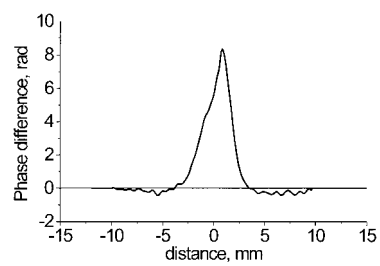

FIG. 5. One-dimensional transverse cross-section through the center of the axial flow velocity map shown in Fig. 4. Each radian of phase difference corresponds to approximately 10 cm/s.

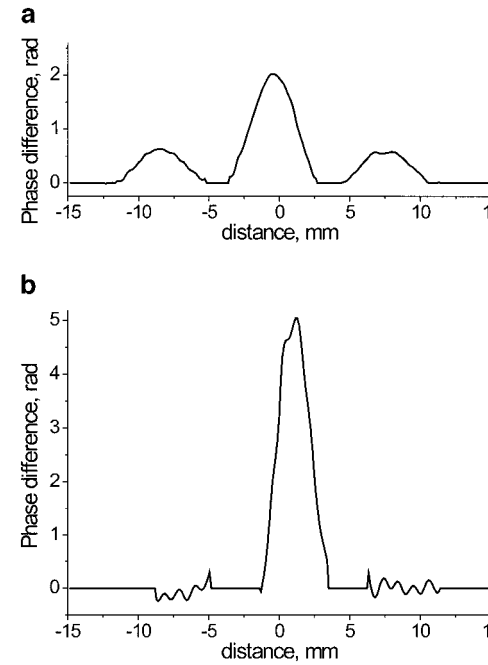

FIG. 9. One-dimensional horizontal cross-sections of the images shown in (a) Fig. 2b for water and (b) Fig. 8 for propane. The positions of the cross-sections are indicated with the solid lines in the respective 2D images.

The spatial resolution of the images detected is 2.5 to 4 times larger than these estimates.

The relaxation times of gases imaged are given in Table 1. The T_1 and T_2 times are rather long and approach those of common liquids as the size of the gas molecule increases. The long T_1 times eliminate one of the advantages of some gas imaging, namely the possibility of using very short repetition times for rapid data averaging (*12*). The large value of T_2 time might be an asset for spectroscopic studies, but has little to contribute to the imaging modality, unless the center of *k*-space is imaged without any applied gradients, as in SPI and SPRITE techniques (*16*).

In spin and gradient echo sequences fast diffusion in the applied gradient attenuates the signal much faster than spin–spin relaxation does. As mentioned earlier, an attempt to increase spatial resolution by doubling the frequency encoding gradients used in this work led to a complete echo dephasing despite the echo times being much shorter than the measured T_2 times. Thus, we are at the upper limit of the gradient and encoding time combination for detecting signals from these rapidly diffusing gases.

Some signal enhancement can be achieved by using the gases at elevated pressures, which will reduce the diffusivity and increase the spin density. This approach is limited by the fact that propane and especially butane liquefy at relatively low pressures (ca. 8.3 atm for propane and 2 atm for *n*-butane at 20°C). Furthermore, T_1 is bound to increase further as the pressure is raised and working at any pressure other than ambient complicates the experiment.

One other possible area of applications of the experiments reported here is the study of porous media. Adsorption of gases within the pores can lead to a substantial signal enhancement (*17*). Furthermore, the restrictions on diffusive displacements of gas molecules provided by the pore walls can reduce the diffusive echo attenuation. It has been demonstrated before that restricted diffusion of gases can be used to selectively suppress the signal of the bulk gas and to obtain images of the gas confined within the pores (*22*). On the other hand, paramagnetic impurities in the pore walls can enhance both T_1 and T_2 relaxation to such a degree that the NMR signal disappears. It is not obvious which way the relaxation times of gases permeating porous materials should change. Both T_1 decreases (*16*) and increases (*17*) for gases in porous materials compared to bulk values have been reported. However, signals from gas or water permeating the porous walls of the monoliths were not observed in this work. The porosity of the monoliths alone would suggest a fourfold reduction of the signal within the walls compared to the bulk fluid, but the actual signal reduction exceeds an order of magnitude. A possible reason for such behavior is a very short T_2^* within the pores, due to paramagnetic impurities in alumina for the samples studied in this work. Indeed, in the previous studies where the drying of these monoliths saturated with water was investigated (*23*), the SPI technique with an encoding time shorter than 1 ms had to be used in order to observe signals from water in pores.

CONCLUSIONS

This work demonstrates that it is not necessary to use hyperpolarized gases or to work at elevated pressures in order to successfully image spatial distributions of gas flow velocities. To the best of our knowledge, this is the first time that NMR gas flow velocity maps of thermally polarized gases have been detected. The spin-warp imaging sequence in combination with flow velocity phase encoding by a pair of magnetic field gradients allowed us to achieve a 400-μm true in-plane spatial resolution in two-dimensional ^{1}H NMR flow velocity images of a 15-mm slice for acetylene, propane, and butane gases. Velocities up to 93 cm/s were measured in this study. Attempts were not made to reduce the slice thickness, but the large signal-to-noise ratio of the images shows that a significant reduction in slice thickness can be tolerated. We applied gas and water flow imaging to measure the flow velocity patterns in the channels of monolithic catalysts. The highly nonuniform distribution of shear rates observed should have a profound influence on mass transfer between the fluids flowing through the channels and pore spaces of shaped catalysts.

ACKNOWLEDGMENTS

The collaboration between the International Tomography Center and New Mexico Resonance was supported by NATO Collaborative Linkage Grant PST.CLG 975244. I.V.K. thanks the Russian Foundation for Basic Research (Project 99-03-32314a) and the Siberian Division of the Russian Academy of Sciences for financial support of this work, and O.P. Klenov (Boreskov Institute of Catalysis) for the samples of monoliths and useful discussions. Additional support by the Engineering Research Program of the Office of Basic Energy Sciences, U. S. Department of Energy, under Grant DE-FG03-98ER14912 is acknowledged.

REFERENCES

1. F. Kapteijn, J. J. Heiszwolf, T. A. Nijhuis, and J. A. Moulijn, Monoliths in multiphase catalytic processes—Aspects and prospects, *CATTECH* **3,** 24–41 (1999).
2. J. Votruba, O. Mikus, K. Nguen, V. Hlavacek, and J. Skrivanek, Heat and mass transfer in honeycomb catalysts—II, *Chem. Eng. Sci.* **30,** 201–206 (1975).
3. P. T. Callaghan, "Principles of Nuclear Magnetic Resonance Microscopy," Clarendon Press, Oxford, (1995).
4. E. Brunner, M. Haake, L. Kaiser, A. Pines, and J. A. Reimer, Gas flow MRI using circulating laser-polarized ^{129}Xe, *J. Magn. Reson.* **138,** 155–159 (1999).
5. M. S. Albert, G. D. Cates, B. Driehuys, W. Happer, B. Saam, C. S. Springer, and A. Wishnia, Biological magnetic resonance imaging using laser-polarized ^{129}Xe, *Nature* **370,** 199–201 (1994).
6. M. E. Wagshul, T. E. Button, H. F. Li, Z. Liang, C. S. Springer, K. Zhong, and A. Wishnia, In vivo MR imaging and spectroscopy using hyperpolarized ^{129}Xe, *Magn. Reson. Med.* **36,** 183–191 (1996).
7. K. Sakai, A. M. Bilek, E. Oteiza, R. L. Walsworth, D. Balamore, F. A. Jolesz, and M. S. Albert, Temporal dynamics of hyperpolarized

^{129}Xe resonances in living rats, *J. Magn. Reson. B* **111,** 300–304 (1996).

8. H. Middleton, R. D. Black, B. Saam, G. D. Cates, G. P. Cofer, R. Guenther, W. Happer, L. W. Hedlund, G. A. Johnson, K. Juvan, and J. Swartz, MR imaging with hyperpolarized ^{3}He gas, *Magn. Reson. Med.* **33,** 271–275 (1995).
9. G. A. Johnson, G. Cates, X. J. Chen, G. P. Cofer, B. Driehuys, W. Happer, L. W. Hedlund, B. Saam, M. D. Shattuck, and J. Swartz, Dynamics of magnetization in hyperpolarized gas MRI of the lung, *Magn. Reson. Med.* **38,** 66–71 (1997).
10. M. Ebert, T. Grossmann, W. Heil, W. E. Otten, R. Surkau, M. Leduc, P. Bachert, M. V. Knopp, L. R. Schad, and M. Thelen, Nuclear magnetic resonance imaging with hyperpolarized helium-3, *Lancet* **347,** 1297–1299 (1996).
11. P. Bachert, L. R. Schad, M. Bock, M. V. Knopp, M. Ebert, T. Grossmann, W. Heil, D. Hofmann, R. Surkau, and E. W. Otten, Nuclear magnetic resonance imaging of airways in humans with use of hyperpolarized ^{3}He, *Magn. Reson. Med.* **36,** 192–196 (1996).
12. D. O. Kuethe, A. Caprihan, E. Fukushima, and R. A. Waggoner, Imaging lungs using inert fluorinated gases, *Magn. Reson. Med.* **39,** 85–88 (1998).
13. P. A. Rinck, S. B. Petersen, and P. C. Lauterbur, NMR-imaging von fluorhaltigen Substanzen, *Fortschr. Roentgenstr.* **140,** 239–243 (1984).
14. F. Kober, B. Koenigsberg, V. Belle, M. Viallon, J. L. Veviel, A. Delon, A. Ziegler, and M. Decorps, NMR imaging of thermally polarized He-3 gas, *J. Magn. Reson.* **138,** 308–312 (1999).
15. Y.-Q. Song, H. C. Gaede, T. Pietrass, G. A. Barrall, G. C. Chingas, G. C. Ayers, and A. Pines, Spin-polarized ^{129}Xe gas imaging of materials, *J. Magn. Reson. A* **115,** 127–130 (1995).
16. P. J. Prado, B. J. Balcom, I. V. Mastikhin, A. R. Cross, R. L. Armstrong, and A. Logan, Magnetic resonance imaging of gases: A single-point ramped imaging with T_1 enhancement (SPRITE) study, *J. Magn. Reson.* **137,** 324–332 (1999).
17. M. J. Lizak, M. S. Conradi, and C. G. Fry, NMR imaging of gas imbibed into porous ceramic, *J. Magn. Reson.* **95,** 548–557 (1991).
18. D. M. Gregory, R. E. Gerald II, and R. E. Botto, Pore-structure determinations of silica aerogels by ^{129}Xe NMR spectroscopy and imaging, *J. Magn. Reson.* **131,** 327–335 (1998).
19. C. H. Tseng, G. P. Wong, V. R. Pomeroy, R. W. Mair, D. P. Hinton, D. Hoffmann, R. E. Stoner, F. W. Hersman, D. G. Cory and R. L. Walsworth, Low-field MRI of laser polarized noble gas, *Phys. Rev. Lett.* **81,** 3785–3788 (1998).
20. A. Caprihan and E. Fukushima, Flow measurements by NMR, *Phys. Rep.* **198,** 195–235 (1990).
21. Landolt-Börnstein, "Zahlenwerte und Funktionen aus Physik, Chemie, Astronomie, Geophysik und Technik", II Band, 5 Teil, Bandteil a, Transportphaenomene I, S. 516. Springer-Verlag, Berlin, 1969.
22. Y.-Q. Song, B. M. Goodson, B. Sheridan, T. M. de Swiet, and A. Pines, Effects of diffusion on magnetic resonance imaging of laser-polarized xenon gas, *J. Chem. Phys.* **108,** 6233–6239 (1998).
23. I. V. Koptyug, R. Z. Sagdeev, L. Yu. Khitrina, and V. N. Parmon, A nuclear magnetic resonance microscopy study of mass transport in porous materials, *Appl. Magn. Reson.* **18,** 13–28 (2000).